The Astrophysical Journal, 744:189 (9pp), 2012 January 10 doi:10.1088/0004-637X/744/2/189

A HIGH STELLAR OBLIQUITY IN THE WASP-7 EXOPLANETARY SYSTEM*

Simon Albrecht[1], Joshua N. Winn[1], R. Paul Butler[2], Jeffrey D. Crane[3], Stephen A. Shectman[3], Ian B. Thompson[3], Teruyuki Hirano[1,4], and Robert A. Wittenmyer[5]

[1] Department of Physics, and Kavli Institute for Astrophysics and Space Research, Massachusetts Institute of Technology, Cambridge, MA 02139, USA
[2] Department of Terrestrial Magnetism, Carnegie Institution of Washington, 5241 Broad Branch Road NW, Washington, DC 20015, USA
[3] The Observatories of the Carnegie Institution of Washington, 813 Santa Barbara Street, Pasadena, CA 91101, USA
[4] Department of Physics, The University of Tokyo, Tokyo 113-0033, Japan
[5] Department of Astrophysics, School of Physics, University of NSW, 2052, Australia

Received 2011 October 26; accepted 2011 November 19; published 2011 December 22

ABSTRACT

We measure a tilt of $86^\circ \pm 6^\circ$ between the sky projections of the rotation axis of the WASP-7 star and the orbital axis of its close-in giant planet. This measurement is based on observations of the Rossiter–McLaughlin (RM) effect with the Planet Finder Spectrograph on the Magellan II telescope. The result conforms with the previously noted pattern among hot-Jupiter hosts, namely, that the hosts lacking thick convective envelopes have high obliquities. Because the planet's trajectory crosses a wide range of stellar latitudes, observations of the RM effect can in principle reveal the stellar differential rotation profile; however, with the present data the signal of differential rotation could not be detected. The host star is found to exhibit radial-velocity noise ("stellar jitter") with an amplitude of $\approx$30 m s^{-1} over a timescale of days.

Key words: planetary systems – planets and satellites: formation – planet–star interactions – stars: individual (WASP-7) – stars: rotation – techniques: spectroscopic

Online-only material: color figure

1. INTRODUCTION

In the solar system the Sun's equatorial plane is aligned to within 7° with the ecliptic. For many stars in systems with close-in gas giants ("hot-Jupiters"), this is not the case. Over the last three years it was found that some hot Jupiters have highly inclined or even retrograde orbits with respect to the rotational spins of their host stars (see, e.g., Hébrard et al. 2008; Winn et al. 2009; Johnson et al. 2009; Triaud et al. 2010; Winn et al. 2011; Simpson et al. 2011). Understanding what causes these orbital tilts and why some hot Jupiters are well aligned with their parent stars might aid our understanding of why these giant planets are found so close to their host stars, compared to Jupiter.

Different classes of processes have been proposed which might transport giant planets from their presumed birthplaces at distances of many astronomical units from their host stars, inward to a fraction of an astronomical unit, where we find them. Some of these processes are expected to change the relative orientation between the stellar and orbital spin (e.g., Nagasawa et al. 2008; Fabrycky & Tremaine 2007; Chatterjee et al. 2008), while others will conserve the relative orientation between orbital and stellar spin (e.g., Lin et al. 1996), or even reduce a misalignment between them (Cresswell et al. 2007).

Winn et al. (2010) and Schlaufman (2010) found that close-in giant planets tend to have orbits aligned with the stellar spin if the effective temperature ($T_{\rm eff}$) of their host star is $\lesssim$6250 K and misaligned otherwise. Winn et al. (2010) further speculated that this might indicate that *all* giant planets are transported inward by processes that create large obliquities. In this picture, tidal torques exerted on the star by the close-in planet realign the two angular momentum vectors. The realignment timescale would be short for planets around stars with convective envelopes ($T_{\rm eff} \lesssim 6250$ K), but long if the star does not have a convective envelope ($\gtrsim$6250 K). Adding to this picture, Triaud (2011) recently argued that relatively young stars have high obliquities, while older stars are observed to have low obliquities.

Here we present measurements of the spin–orbit angle in the WASP-7 system. The planet WASP-7b was discovered by Hellier et al. (2009) and found to have a mass of 0.96 $M_{\rm Jup}$. The host star has a mass of 1.28 $M_\odot$, a projected rotation speed of 17 ± 2 km s^{-1} (Hellier et al. 2009), an effective temperature of 6520 ± 70 K, and a solar metallicity ([Fe/H] $= 0.0 \pm 0.1$) (Maxted et al. 2011). Based on the aforementioned pattern, we would expect that our measurement would show a misalignment between orbital and stellar spins.

This article is organized as follows. The following section describes the new spectroscopic data and the analysis of the Rossiter–McLaughlin (RM) effect. Section 4 considers some possible explanations for the high level of noise in the radial velocities, including the possibility of an eccentric orbit. Section 5 discusses the impact of the radial-velocity (RV) noise on the measurement of the stellar obliquity. This section also presents an attempt to detect the differential rotation of the host star using the RM effect.

2. OBSERVATIONS

We observed WASP-7 with the Magellan II (Clay) 6.5 m telescope and the Planet Finder Spectrograph (PFS; Crane et al. 2010). We gathered 37 spectra spanning the transit of 2010 August 27/28. The integration times were 10 minutes and the complete sequence spanned ~7.5 hr. The stellar spectra were observed through an iodine gas cell, imprinting a dense forest of sharp absorption lines on the stellar spectra to help establish the wavelength scale and instrumental profile. During the transit night, an additional spectrum was obtained without the iodine cell, to serve as a template spectrum for relative RV determination.

* The data presented herein were collected with the Magellan (Clay) Telescope located at Las Campanas Observatory, Chile.

Table 1
Relative Radial Velocity Measurements of WASP-7

Time (BJD_{TDB})	RV ($m\ s^{-1}$)	Uncertainty ($m\ s^{-1}$)
2455436.50918	108.47	6.02
2455436.51698	97.80	6.86
2455436.52487	88.78	6.66
2455436.53284	98.31	6.28
2455436.54061	101.71	6.31
2455436.54849	77.67	5.68
2455436.56752	95.27	5.95
2455436.60407	63.98	5.07
2455436.61195	51.13	5.92
2455436.61959	55.06	5.16
2455436.62746	56.87	5.15
2455436.63541	66.72	4.97
2455436.64327	39.04	5.03
2455436.65130	51.37	4.76
2455436.65906	16.99	5.37
2455436.66704	−35.49	5.24
2455436.67499	−10.86	4.60
2455436.68278	−33.56	5.03
2455436.69064	−41.08	5.37
2455436.69864	−56.32	5.84
2455436.70650	−46.43	5.79
2455436.71432	−58.03	5.09
2455436.72230	−65.73	5.53
2455436.73005	−55.67	5.25
2455436.73790	−69.74	5.35
2455436.74578	−58.04	4.88
2455436.75369	−51.82	5.56
2455436.76152	−58.06	5.81
2455436.76939	−61.90	6.08
2455436.77732	−55.81	6.02
2455436.78511	−17.29	5.70
2455436.79311	−30.23	5.88
2455436.80081	−11.96	6.73
2455436.80882	20.31	6.76
2455436.81669	11.38	6.45
2455436.82451	0.00	6.81
2455436.83244	28.73	7.09

3. ANALYSIS OF THE ROSSITER–MCLAUGHLIN EFFECT

To derive the relative RVs we compared the spectra observed through the iodine cell with the stellar template spectrum multiplied by an iodine template spectrum. The velocity shift of the stellar template as well as the parameters of the point-spread function (PSF) of the spectrograph are free parameters in this comparison. The velocity shift of the template that gives the best fit to an observed spectrum represents the measured relative RV. In particular we used a code based on that of Butler et al. (1996). The RVs are presented in Table 1 and displayed in Figure 1.

We take advantage of the RM effect to measure the projected angle between the orbital and stellar spins (λ) and the projected stellar rotation speed ($v \sin i_\star$). Here v indicates the stellar rotation speed and $i_\star$ indicates the inclination of the stellar spin axis toward the observer. The RM effect is a spectroscopic distortion of the rotationally broadened stellar absorption lines, which occurs when a companion star or planet is in front of the star and hides part of the rotating stellar surface from the observer's view. The position of the distortion on the stellar absorption line depends on the RV of the hidden portion of the stellar surface. Therefore, the observed distortion of the stellar absorption lines can be connected to the geometry of the transit. This shape change can be measured directly and relevant parameters can be derived (Albrecht et al. 2007; Collier Cameron et al. 2010).

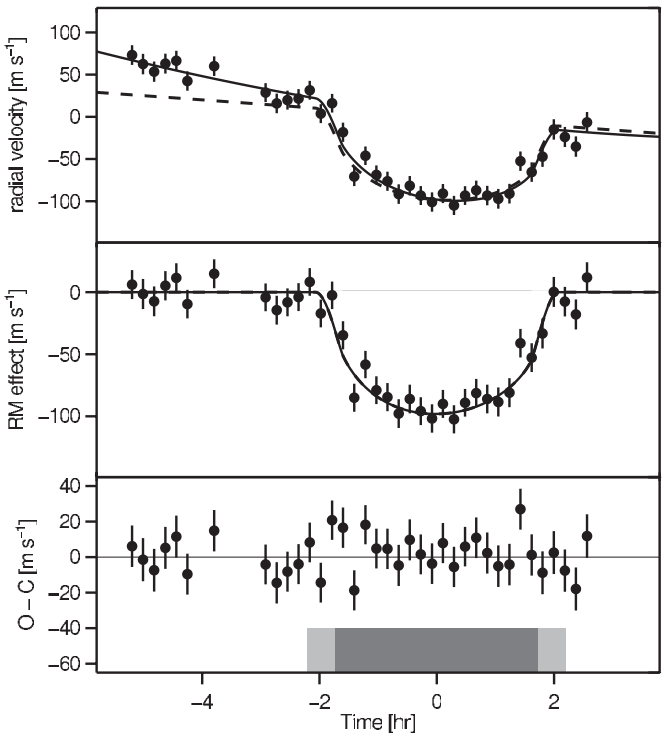

Figure 1. Radial velocities of WASP-7 before, during, and after the transit of its planet. The radial velocities are plotted as a function of time from inferior conjunction. The upper panel shows the measured RVs and the best-fitting model. The dashed line shows the same RM model, but with an orbital model with parameters fixed at those presented by (Hellier et al. 2009; see also Section 4). In the middle panel, the apparent orbital contribution to the observed RVs has been subtracted, thereby isolating the RM effect. The lower panel shows the residuals. The light and dark gray bars in the lowest panel indicate times of first, second, third, and fourth contact.

Our analysis is divided into seven parts. In Section 3.1, we discuss the data qualitatively. Sections 3.2–3.6 discuss different phenomena which affect the shape of stellar absorption lines. Section 3.7 discusses the model of the RM effect which we adopted, and presents the quantitative results.

3.1. Qualitative Expectations

The RM effect is evident in Figure 1 as the large negative velocity excursion (blueshift) that was observed throughout the transit. The effect was observed with a high signal-to-noise ratio. Simply from the observation that the effect is a blueshift throughout the transit, we may obtain some information on the spin–orbit alignment of the system. A qualitative discussion will help in understanding the quantitative analysis to be discussed later in this paper.

If the projections of the stellar and orbital spins were aligned, then the planet would first traverse the half of the stellar surface for which the rotation velocity has a component directed toward the observer (blueshifted). The blockage of a portion of this blueshifted half of the star would cause the absorption lines to appear slightly redshifted. Then, in the second half of the transit, the reverse would be true: the anomalous RV would be a blueshift. In contrast, the RM effect was observed to be a blueshift throughout the transit. This implies that the planet's trajectory is entirely over the redshifted half of the star.

The symmetry of the RM signal about the midtransit time provides further information. For a star in uniform rotation, the line-of-sight (LOS) component of the rotation velocity at any point on the photosphere is proportional to the distance from the projected rotation axis; see, e.g., pp 461–462 of Gray (2005). Therefore, if the planet's trajectory is at a constant distance from the projected rotation axis (i.e., if the projected orbital and spin axes are perpendicular), the hidden velocity component will be nearly constant in time and the only variation in the RM signal arises from limb darkening, which is symmetric about the midtransit time. In fact this is the only way to produce a time-symmetric RM effect unless the impact parameter is nearly zero, which is not the case for WASP-7 (Southworth et al. 2011).

We conclude that the projected orbital and spin axes are nearly perpendicular, and since the anomalous RV is a blueshift we expect $\lambda \approx 90^\circ$ (as opposed to -90°), using the coordinate system of Ohta et al. (2005). This qualitative conclusion is confirmed by our quantitative analysis discussed below; but first we must take into account several effects besides rotation that influence the shape of the measured absorption lines.

3.2. Line Broadening and the Impact on the Analysis

Stellar absorption lines are broadened not only by the Doppler shifts due to stellar rotation, but also by random motions of material on the visible stellar surface. These random motions are often referred to as microturbulence and macroturbulence, depending on whether the length scale of the velocity field is smaller or larger than the length scale over which the optical depth is of order unity (see, e.g., Gray 2005). In this picture, the influence of microturbulence can be described by a simple convolution by a Gaussian function of an appropriate width with the rotationally broadened stellar lines. The effect of the macroturbulence depends on the angle between the LOS and the local normal to the stellar surface. Near the center of the stellar disk, the Doppler shifts are produced mainly by motions that are radial with respect to the stellar center; whereas near the stellar limb, the Doppler shifts are produced by motions tangential to the stellar surface. Therefore, modeling this effect requires a spatial integration over the visible hemisphere. For this purpose we employ the semi-analytical approach of Hirano et al. (2011b).

Other contributions to the line width come from collisional broadening and Zeeman splitting. These effects are small for WASP-7 compared to the other effects, and we describe them by the convolution of the disk-integrated line profiles with a Lorentzian function of width 1 km s^{-1}.

3.3. Convective Blueshift

Another potentially relevant effect on line profiles is the convective blueshift. At the top of a convective cell, where it meets the photosphere, the rising material is hotter and therefore more luminous than the sinking material. Due to the dominance of the rising material over the falling material, an observer placed vertically above the stellar surface would detect an overall net blueshift in the integrated light. This effectively outward RV is referred to as the convective blueshift. When integrating over the visible stellar disk, the convective blueshift from the center of the disk has a maximal effect on the observed RV, while the convective blueshift from points near the stellar limb have a weaker effect because the outward RV has only a small component along the LOS. Thus, the influence of the convective blueshift is strongest near the center of the line profile and weaker in the wings of the lines where a substantial portion of the light originates from the stellar limb.

Therefore, the disk-integrated light has not only an overall Doppler shift but also an asymmetry in the stellar absorption lines. To describe this, we employ the model of Shporer & Brown (2011). This model captures the first-order effects of the convective blueshift but ignores a higher-order asymmetry in the absorption lines: the line cores are formed relatively high in the photosphere where turbulent motions may be less important. As WASP-7 is a relatively hot star, with high turbulent velocities, it seems appropriate to ignore the latter effect (see Figure 17.15 in Gray 2005).

3.4. Differential Rotation

When analyzing the RM effect researchers normally assume the eclipsed star is rotating uniformly (no differential rotation). In the case of WASP-7, the planet's trajectory is evidently perpendicular to the projected stellar equator (see Section 3.1), and therefore spans a wide range of stellar latitudes, and the effects of differential rotation might be expected to be especially important. Ignoring the possibility of differential rotation might lead to a systematic error in the measurement of the projected obliquity. For a well-aligned system ($\lambda \approx 0^\circ$) the effect is much less important because the planet probes only a small range of stellar latitudes over the course of the transit (see also Gaudi & Winn 2007).

We have limited empirical knowledge of differential rotation profiles in stars other than the Sun, and therefore we have limited ability to predict the impact of differential rotation on our observation of WASP-7. One relevant study is by Reiners & Schmitt (2003), who examined differential rotation in slowly rotating stars ($v \sin i_\star \lesssim 20$ km s^{-1}). In their sample, all stars having a $\log R'_{HK}$ index between -4.80 and 4.65 showed signs of differential rotation, while more active stars had no discernible differential rotation. Their sample did not include any quieter stars ($\log R'_{HK} < -4.80$). In this context, we should expect significant differential rotation for WASP-7, which rotates more slowly than 20 km s^{-1} (Hellier et al. 2009), and has a low activity index $\log R'_{HK}$ of -4.981 (H. Knutson, 2011, private communication). We adopt the parameterization used by Reiners & Schmitt (2003) and others,

$$\Omega(l) = \Omega_{\rm eq}(1 - \alpha \sin^2 l). \quad (1)$$

Here l denotes stellar latitude and $\Omega_{\rm eq}$ denotes the angular rotation speed at the equator. α is a dimensionless parameter which describes the degree of differential rotation. An α of 0 would indicates uniform rotation and an α of 0.2 corresponds to Sun-like differential rotation. See also Hirano et al. (2011a), who used the RM effect to set an upper limit on the stellar differential rotation in the XO-3 system.

3.5. Modeling the Anomalous RV

In order to develop a model for the anomalous RV produced by the RM effect, we must take into account two other effects: (1) the stellar absorption lines recorded by the spectrograph are further broadened by the PSF of the spectrograph; and (2) the measured RVs represent the output of a Doppler-measuring code, which is akin to finding the peak of a cross-correlation between a stellar template spectrum obtained outside the transit, and a spectrum observed during the transit. Some researchers neglect the second point, and model the anomalous RV as the shift in the first moment of the model absorption line rather

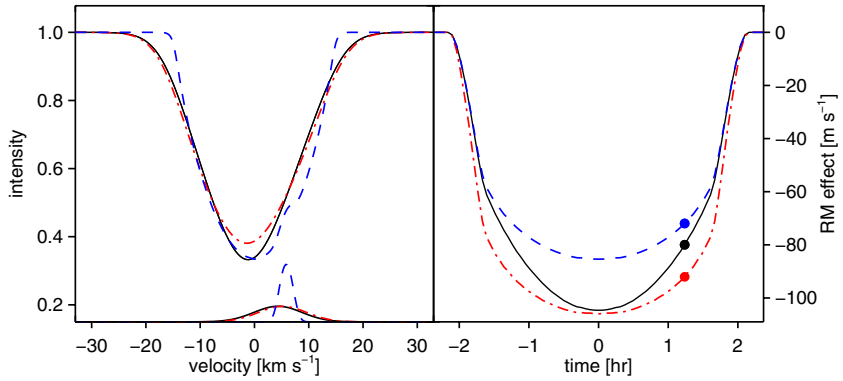

Figure 2. Line broadening mechanisms and their influence on the RM effect. Left: model absorption line exhibiting the RM effect. The blue dashed line shows the idealized case in which the only line broadening mechanism is uniform rotation. The red dash-dotted line shows the case in which macroturbulence and the convective blueshift are also taken into account. The black line shows the case in which the former effects as well as differential rotation are taken into account. The lower set of lines indicate the "loss of light" in the stellar absorption line due to shadowing by the planet. For visibility this was multiplied by a factor of three. These models are based on the parameters given in Table 2. Right: time variation of the RM effect (anomalous RV) for the same models as in the left panel. The circles indicate the particular phase for which the model line profiles in the left panel are shown. While the shift in the first moment appears to be larger for the blue dashed line (left panel) than for the other lines, its RM effect is smaller (right panel). This is partly a result of the measurement technique as described in Section 3.5. In addition, the black and red dash-dotted lines are influenced by the convective blueshift (Section 3.3).

(A color version of this figure is available in the online journal.)

than as the shift in the peak of the cross-correlation function. Depending on the system parameters this can lead to systematic errors in the derived parameters (Hirano et al. 2010, 2011b).

Hirano et al. (2011b) developed an analytical description for the shift in the cross-correlation peak as a function of the transit parameters, the stellar rotation velocity and obliquity, the microturbulent and macroturbulent velocities, the differential rotation profile, and the PSF width of the spectrograph. We use their approach to model the obtained RVs during transit and also include a model as described above for the convective blueshift. See Figure 2 for an illustration of how the above-described effects change the line shape and the time variation of the RM effect.

3.6. Other RV Variation Sources

To this point we have only discussed changes in the RVs due to the transit. To successfully model the RM effect we also need to model the change in RV due to the orbital motion of the star. In addition, as we will see in Section 4, WASP-7 shows a high level of RV noise on a timescale of days, which will introduce trends in the RV over the course of the transit night. Therefore, our model allows for RV trends that are linear or quadratic functions of time, in addition to the RM effect and orbital motion. The physical interpretation of these trends is discussed in Section 4.

3.7. Quantitative Analysis

Now that all the ingredients of our model have been introduced, we describe the various parameters in detail. The Keplerian orbital motion of the star is specified by the period (P), the time of inferior conjunction (T_c), the semi-amplitude of the projected stellar reflex motion ($K_\star$), and a velocity offset (γ). Initially we assume the orbit to be circular, as Hellier et al. (2009) found no sign of an orbital eccentricity (although see Section 4). We also allow for additional linear and quadratic RV trends (a_1 and a_2) on the transit night,

$$\mathrm{RV}(t) = \gamma + \mathrm{RV}_{\mathrm{Orbit}}(t) + \mathrm{RV}_{\mathrm{RM}}(t) + a_1 * (t - t_0) + a_2 * (t - t_0)^2 \quad . \quad (2)$$

Here $\mathrm{RV}_{\mathrm{Orbit}}(t)$ and $\mathrm{RV}_{\mathrm{RM}}(t)$ represent the radial velocities caused by the orbital motion and the RM effect. t_0 is a point in time near the middle of our observation sequence. Since allowing for these trends we have relinquished any power to constrain $K_\star$ with the data, so we fix $K_\star$ at the value reported by Hellier et al. (2009).

The amount of light blocked at any given phase of the transit depends on the location of the chord of the planet's path over the stellar disk, which is parameterized by the cosine of the orbital inclination ($\cos i_o$), the radius of the star in units of the orbital semimajor axis ($R_\star/a$), and the radius of the planet relative to the stellar radius ($R_p/R_\star$). We use quadratic limb-darkening parameters u_{1rm} and u_{2rm} to parameterize the relative intensity of the stellar surface in the wavelength region of 5000–6200 Å, the spectral region in which the RVs are measured. We chose limb-darkening coefficients $u_{1rm} = 0.3$, $u_{2rm} = 0.35$, based on the tables of Claret (2004). We allowed $u_{1rm} + u_{2rm}$ to vary freely and held fixed $u_{1rm} - u_{2rm}$ at the tabulated value of -0.05, since the difference is only weakly constrained by the data (and in turn has little effect on the other parameters).

We parameterize the projected spin–orbit angle and the projected stellar rotation by the quantities $\sqrt{v \sin i_\star} \cos \lambda$ and $\sqrt{v \sin i_\star} \sin \lambda$, rather than $v \sin i_\star$ and λ. We do this because our chosen parameters are less strongly correlated (e.g., Albrecht et al. 2011). Our macroturbulence model was that of Gray (2005), assuming equal surface fractions of radial and tangential velocities, with a macroturbulence parameter ζ subject to a Gaussian prior of $6.4 \pm 1.0\,\mathrm{km\,s^{-1}}$. This represents our expectation for a star of WASP-7's effective temperature (Gray 1984). To model the convective blueshift we assumed an outward blueshift of $1\,\mathrm{km\,s^{-1}}$ at all positions on the star (Shporer & Brown 2011, and references therein). We further include α, the parameter which governs the strength of differential rotation, and the stellar inclination toward the observer ($i_\star$) as free parameters. As Reiners & Schmitt (2003) found no star with $\alpha \sqrt{\sin i_\star}$ greater ≈ 0.4 (see their Figure 16) we also impose a prior on α which is flat until 0.4 and then falls off as a Gaussian function with a standard deviation of 0.1.

Finally, we must specify the width of a Gaussian function representing the width of the lines due to both microturbulence and the PSF of the spectrograph. We chose $\sigma = 3\,\mathrm{km\,s^{-1}}$ for this purpose. Also, to represent the natural broadening of the

Table 2
Parameters of the WASP-7 System

Parameter	Values
Parameters mainly derived from photometry	
Midtransit time T_c ($BJD_{TDB}-2{,}400{,}000$)	55446.635 ± 0.0003
Period, P (days)	4.9546416 ± 0.0000035
$\cos i_o$	0.05 ± 0.02
Fractional stellar radius, $R_\star/a$	$0.109 \pm {}^{0.011}_{0.006}$
Fractional planetary radius, $R_p/R_\star$	0.096 ± 0.001
u_1+u_2	0.34 ± 0.08
Parameters mainly derived from RVs	
Velocity offset, (m s^{-1})	34 ± 5
Linear slope during transit night, a_1 (m s^{-1})	-95 ± 41
Quadratic slope during transit night, a_2 (m s^{-1} day^{-1})	500 ± 310
$\sqrt{v \sin i_\star}\sin\lambda$ (km s^{-1})	3.7 ± 0.3
$\sqrt{v \sin i_\star}\cos\lambda$ (km s^{-1})	0.24 ± 0.56
Macroturbulence parameter, ζ (km s^{-1})	$6.4 \pm 1.$
u_{1rm}+u_{2rm}	0.92 ± 0.06
Differential rotation parameter, α	0.45 ± 0.11
$\cos i_\star$	0.18 ± 0.43
Indirectly derived parameters	
Orbital inclination, i_o (°)	$87.2 \pm {}^{0.9}_{1.2}$
Full duration, T_{14} (hr)	$4.12 \pm {}^{0.09}_{0.06}$
Ingress or egress duration, T_{12} (minutes)	$27 \pm {}^{6}_{9}$
Projected stellar rotation speed, $v \sin i_\star$ (km s^{-1})	14 ± 2
Projected spin–orbit angle, λ (°)	86 ± 6

lines we used a Lorentzian function with a width of 1 km s^{-1} (see also Hirano et al. 2011b).

Additional information on the transit geometry comes from a transit light curve recently obtained by Southworth et al. (2011). They made their de-trended light curve available via VizieR. They also gave an updated transit ephemeris for the system, which is derived from the WASP discovery data in combination with the new light curve. We used those updated results for P and T_c as priors (see Equation (3)). We also fitted the light curve simultaneously with the RVs in order to pin down $\cos i_o$, $R_\star/a$, and $R_p/R_\star$. We used the algorithm from Mandel & Agol (2002) to model the light curve which was obtained in the Gunn I filter. From Claret (2004) we obtained $u_1 = 0.17$ and $u_2 = 0.36$. We allowed $u_1 + u_2$ to vary freely, and held $u_1 - u_2$ fixed at the tabulated value of -0.19.

To derive confidence intervals for the parameters we used the Markov Chain Monte Carlo (MCMC) algorithm. The likelihood was taken to be $\exp(\chi^2/2)$, where χ^2 was defined as

$$\chi^2 = \sum_{i=1}^{57}\left[\frac{\mathrm{RV}_i(\mathrm{o})-\mathrm{RV}_i(\mathrm{c})}{\sigma_{\mathrm{RV},i}}\right]^2 + \sum_{j=1}^{1134}\left[\frac{\mathrm{F}_j(\mathrm{o})-\mathrm{F}_j(\mathrm{c})}{\sigma_{\mathrm{F},j}}\right]^2 + \left(\frac{T_{c,\mathrm{BJD}}-2455446.63493}{0.000030}\right)^2 + \left(\frac{P-4^{\mathrm{d}}.9546416}{0^{\mathrm{d}}.0000035}\right)^2 + \left(\frac{\zeta-6.425\,\mathrm{km\,s^{-1}}}{1\,\mathrm{km\,s^{-1}}}\right)^2 + \begin{cases}0 & \text{if } \alpha \leqslant 0.4\\ \left(\frac{\alpha-0.4}{0.1}\right)^2 & \text{if } \alpha > 0.4\end{cases}. \quad (3)$$

The first two terms are sums-of-squares over the residuals between the observed (o) and calculated (c) values of the RV and relative flux (F). The following terms represent priors on some parameters, as mentioned above. Before starting the chain

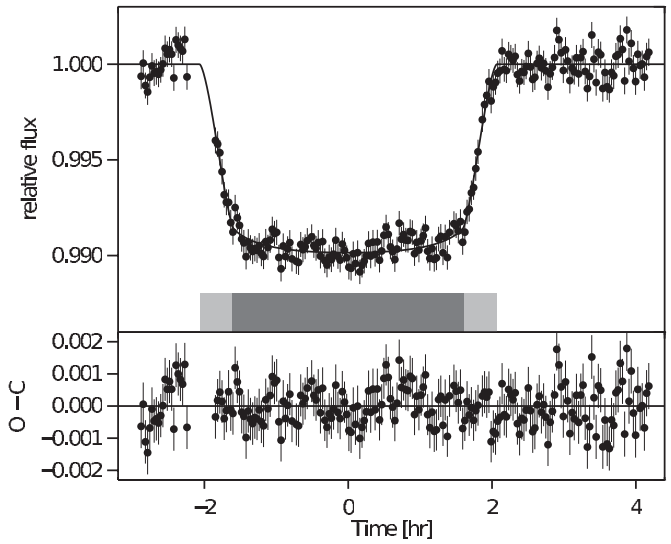

Figure 3. Photometry of WASP-7 transits. The upper panel shows the light curve obtained by Southworth et al. (2011) in the Gunn I filter, and our best-fitting model. The lower panel shows the residuals between the data and best-fitting model.

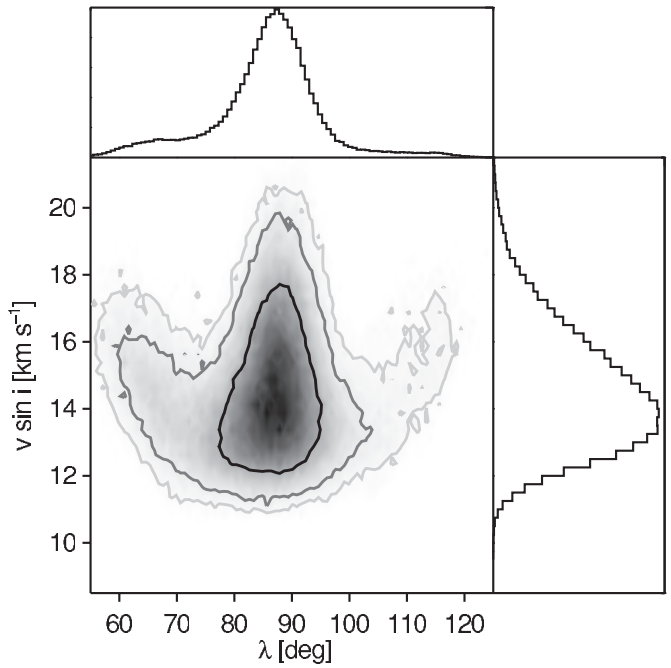

Figure 4. Results for $v \sin i_\star$ and λ, based on our MCMC analysis in the WASP-7 system. The gray scale indicates the posterior probability density, marginalized over all other parameters. The contours represent the two-dimensional 68.3%, 95%, and 99.73% confidence limits. The one-dimensional marginalized distributions are shown on the sides of the contour plot.

we also added 10 m s^{-1} in quadrature to the uncertainty of the PFS RVs to obtain a reduced χ^2 close to unity. In making this step we assumed that the uncertainties in the RV measurements are uncorrelated and Gaussian.

Our results are presented in Table 2. The best fits to the RVs and photometry are shown in Figures 1 and 3. Figure 4 shows the two-dimensional posterior density distribution for the two parameters of greatest interest for our study: λ and $v \sin i_\star$.

For the parameters governed mainly by the photometric data, our results are consistent with those obtained by Southworth et al. (2011). We will discuss the reliability of some of the

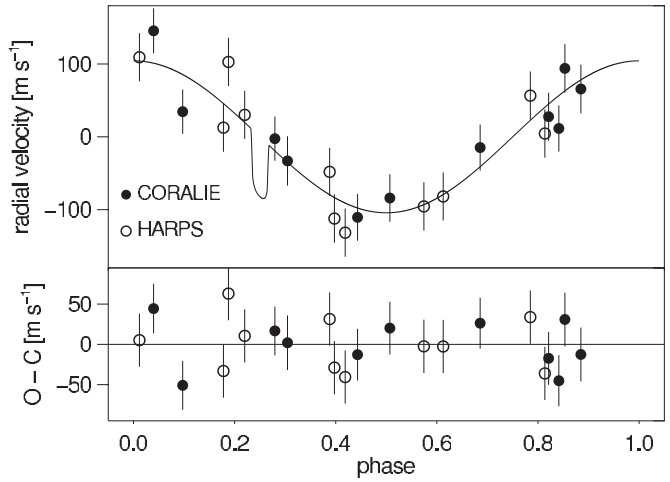

Figure 5. Orbital solution with zero eccentricity for WASP-7. The upper panel shows RV observations as function of the orbital phase, with periastron at zero phase. The CORALIE RVs are indicated by filled symbols and the HARPS data are shown by open symbols. The lower panel shows the residuals between data and best-fitting model.

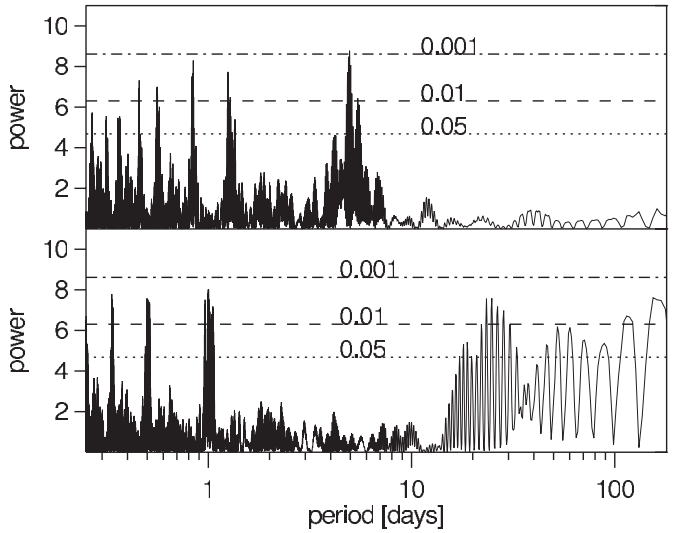

Figure 6. Lomb–Scargle periodograms of the out-of-transit RVs. The upper panel shows the power at different periods in the RV data of the two data sets from CORALIE and HARPS. The highest peak occurs at the orbital period. The lower panel shows the power in the RV data after the best-fitting model was subtracted. Significant peaks occur at a period of one day, and its higher harmonics. Most likely this is a consequence of the diurnal time sampling of the RV observations.

parameters found by the RV data, in particular spectral limb darkening, the evidence for differential rotation, and the stellar inclination in Section 5.1, after investigating possible reasons for the excess noise in the RV data in the following section.

4. STELLAR JITTER AND ORBITAL ECCENTRICITY

The out-of-transit RV gradient measured with the PFS is steeper than would be expected from the previously published spectroscopic orbit. That slope, and the known orbital period, imply an orbital velocity semi-amplitude of $K_\star \approx 200$ m s^{-1}, in strong contrast to the published value of 97 ± 13 m s^{-1}. (See the upper panel in Figure 1.)

Archival RV data from the CORALIE and HARPS spectrographs, obtained during various orbital phases, show a large scatter around the best orbital solution in excess of the measurement uncertainties. This type of excess noise is commonly referred to as "stellar jitter." In the following we will shortly investigate the timescale over which the RV scatter is correlated and test the possibility that the orbit is actually eccentric.

4.1. Excess Noise

We turn first to the previously reported RVs. Eleven measurements were obtained with CORALIE by Hellier et al. (2009) and another 11 RVs were measured with HARPS by Pont et al. (2011). We fitted an orbital model to both data sets separately to determine the root-mean-square (rms) residual between the data and the best-fitting model. A high rms would indicate that our model neglects an effect which influences the RVs, which, for example, could be activity of the star itself. We find that the scatter of both the CORALIE and HARPS RVs is not only greater than what these instruments normally achieve on bright stars, also the rms of the HARPS data (33 m s^{-1}) is slightly higher than the rms of the CORALIE RVs (31 m s^{-1}). This is noteworthy as HARPS should achieve a greater precision than CORALIE, if photon noise is the limiting factor, as HARPS operates in conjunction with a 3.6 m telescope and CORALIE with a 1.2 m telescope. This suggests that an additional source of RV variations may be present, which dominates the noise budget.

Next we fitted each data set individually, assuming a circular orbit and adding a term in quadrature to the internal uncertainties to produce a reduced χ^2 of unity. In making this step we assumed that the errors of the RV measurements are uncorrelated and Gaussian. We needed to add 25 m s^{-1} in quadrature to the internal uncertainties of 11 CORALIE data points and 33 m s^{-1} to the uncertainties of 11 HARPS RVs.

Using those inflated uncertainties, we fitted both data sets together, also assuming a circular orbit. Our fitting statistic was

$$\chi^2 = \sum_{i=1}^{22} \left[\frac{\mathrm{RV}_i(\mathrm{o}) - \mathrm{RV}_i(\mathrm{c})}{\sigma_{\mathrm{RV},i}} \right]^2 + \left(\frac{T_{\mathrm{c,BJD}} - 2455446.63493}{0.000030} \right)^2 + \left(\frac{P - 4^{\mathrm{d}}.9546416}{0^{\mathrm{d}}.0000035} \right)^2, \quad (4)$$

making use of the ephemeris from Southworth et al. (2011).

Figure 5 shows the phase-folded RV data. As expected from the previous fits, the rms residual is 31.4 m s^{-1}. To understand this noise source it would be important to learn the timescale over which the RV noise is correlated. Looking at the Lomb–Scargle periodogram of the RV data, we find the most dominant peak at the orbital period of WASP-7b (Figure 6, upper panel). After subtracting the best-fitting circular-orbit model, the periodogram of the residuals shows a strong peak at a period of one day and its harmonics (Figure 6, lower panel). This is most likely a result of the timing of the observations. Many observations were obtained on consecutive nights. Apart from this pattern, the periodogram is not very informative. An autocorrelation plot does not reveal additional information.

The timing is different for the PFS observations. We obtained 37 data points during an interval of 7.5 hr. The rms around our solution including the orbital model, the linear and quadratic acceleration, and the RM effect is 11 m s^{-1} (Figure 1). This relatively low scatter indicates that the correlation time of the RV variations is longer than a few hours.

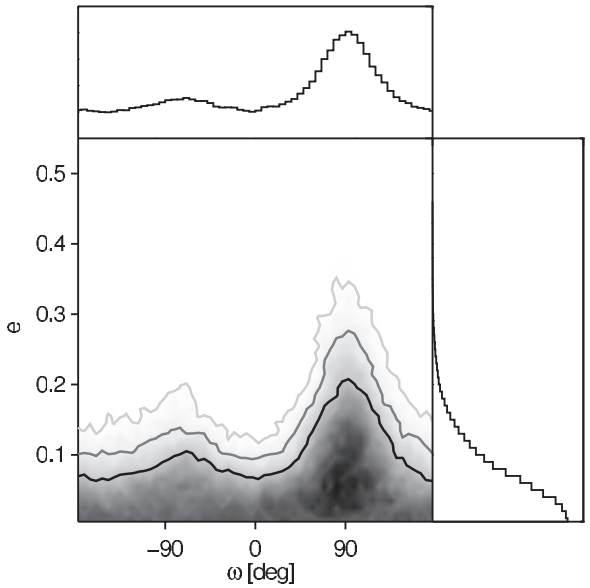

Figure 7. Constraints on the orbital eccentricity (e) and orientation (ω) of WASP-7 from HARPS and CORALIE data. The gray scale indicates the posterior probability density, marginalized over all other parameters. The contours represent the two-dimensional 68.3%, 95%, and 99.73% confidence limits. The eccentricity is constrained to low values. For an orientation of $\omega \approx |90|^\circ$ somewhat higher values of the eccentricity are allowed. That is particularly true for positive value of ω. The one-dimensional marginalized distributions are shown on the sides of the contour plot.

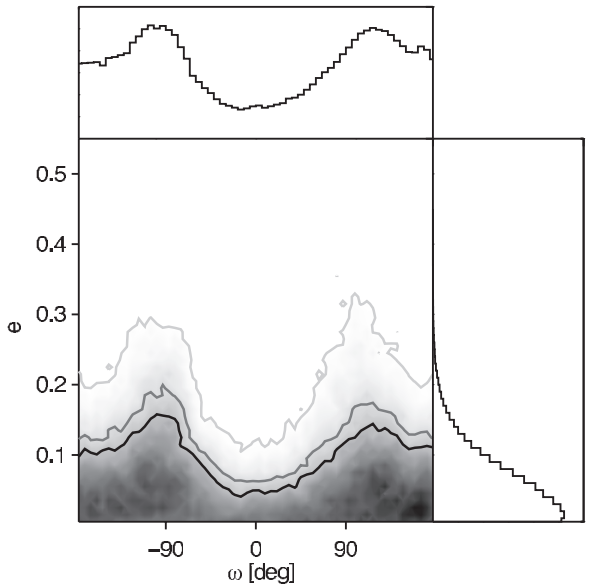

Figure 8. Results for orbital eccentricity using synthetic data. Similar to Figure 7 but this time for an MCMC analysis of a synthetic data set which was derived from a circular-orbit model. The results indicate that higher eccentricities are allowed for ω near 90° or −90°.

We note that WASP-7 is not the only early-type planet host star for which a large stellar jitter has been observed. Recently, Hartman et al. (2011) found that the two-planet host stars in the HAT-P-32 and HAT-P-33 systems have stellar jitter of ≈ 80 and 55 m s^{-1}.

4.2. Orbital Eccentricity

One possible contributing factor to the excess RV noise is that the orbit is actually eccentric, in violation of our modeling assumption of a circular orbit. To investigate this possibility we repeated the MCMC analysis but allowed the orbital eccentricity (e) and the argument of periastron (ω) to be free parameters. Our stepping parameters were $\sqrt{e}\sin\omega$ and $\sqrt{e}\cos\omega$, which have less correlated uncertainties for small eccentricity, and which correspond to a flat prior in e.

Using the likelihood based on Equation (4), we derived the posterior probability, which is displayed in the ω–e plane in Figure 7. The rms for the best-fitting eccentric solution is with 30.9 m s^{-1}, only moderately smaller than for the circular-orbit model. We can see from Figure 7 that there is no clear detection of an eccentric orbit and that solutions with $e \gtrsim 0.2$ are generally disfavored except for values of ω near 90°, for which somewhat larger eccentricities are allowed. Such an argument of periastron would indicate for transiting systems a semimajor axis closely aligned with the LOS. Interestingly, such an orbital orientation would lead to a steeper RV slope during the transit night, which is indeed what was observed with the PFS.

However, the peak in the probability density near $\omega \approx 90^\circ$ should not be taken as evidence that the orbit really does have this orientation. This is probably just the result of the fact that RV studies are better at constraining $\sqrt{e}\times\cos\omega$ than $\sqrt{e}\times\sin\omega$, and consequently we expect the confidence interval for e to be larger for ω close to $|90|^\circ$. Such an orbital configuration would lead to symmetric RV curves even for an eccentric orbit, i.e., the RV amplitudes at the quadratures would not differ.

To investigate this point further we conducted numerical experiments similar to those carried out by Laughlin et al. (2005) for the HD 209458 system. We created simulated RV data sets with the same time stamps as the CORALIE and HARPS data sets. For this we assumed a circular orbit with the parameters of the WASP-7 system. We then added Gaussian perturbations to the model RVs, adopting a 1σ uncertainty of 33 m s^{-1}, and then used the same MCMC analysis for these mock data as was used for the real data sets. A typical two-dimensional posterior resulting from this experiment is shown in Figure 8.

We found that greater values of e are permitted for orbital orientations of $\approx |90|^\circ$. This should make us suspicious of any low-S/N detection of an orbital eccentricity with an ω of $\approx |90|^\circ$. We conclude that the out-of-transit RVs give no indication of an eccentric orbit for WASP-7. This is in line with the upper limit $e < 0.25$ found by Pont et al. (2011). We note that the ω-dependent sensitivity to e is very similar to the $v\sin i_\star$-dependent sensitivity to λ that was explicated by Albrecht et al. (2011), for low-SNR studies of the RM effect. In that case, higher values of the stellar rotation rate ($v\sin i$) are allowed for $\lambda \approx 0^\circ$ and $\approx 180^\circ$, even when the underlying signal has no RM effect at all.

5. DISCUSSION

5.1. Differential Rotation Parameters

Our model took into account the possible effects of differential rotation, through the parameters α and $i_\star$. We found that the upper boundary of the posterior distribution for α is determined mainly by our prior. Specifically we found $\alpha = 0.45 \pm 0.11$, with the prior enforcing $\alpha < 0.5$ (see Table 2). If instead no prior is placed on α, then we found that the differential rotation parameter increases to values as high as 0.9, much higher than would be expected based on theory and on observations of other stars.

This should make us suspicious. For $|\lambda|$ close to 90°, as is the case here, a parameter degeneracy exists between the limb-darkening profile and the degree of differential rotation, because both of those phenomena produce changes to the RM effect that are symmetric in time about the transit midpoint. Perhaps our assumptions are mistaken regarding the stellar limb darkening within the effective observing bandpass. For RM observations the effective observing bandpass is complicated to describe, depending as it does upon the density of I_2 absorption lines. Furthermore, there may be systematic differences between the limb darkening as observed in different absorption lines, and even within a single strong line, as different parts of the absorption lines form in different depths of the stellar photosphere. Nevertheless, the fitted value of the center-to-limb variation ($u_{1rm} + u_{2rm} = 0.92 \pm 0.06$) is already quite high; lowering this value would only cause α to converge to *larger* values.

The data seem to be demanding a greater variation of the RM effect between the second and third contact than is delivered by the expected amounts of limb darkening and differential rotation. Some possible explanations are as follows.

1. The stellar jitter exhibits correlations on the timescale of minutes to hours, which is not taken into account in our model. By fitting a linear and quadratic trend to the RVs, we have only taken into account correlations on longer timescales.
2. If WASP-7 is pulsating then velocity fields on the stellar surface, due to the pulsations, might lead to a different shape of the stellar absorption line than is created by our model, which does not include pulsations. The planet would occult during its transit different velocity components than expected. For this effect to be important the velocity fields do not need to change on a timescale comparable to the transit.
3. Another possibility is that our model of the convective blueshift is not correct. For hotter stars there exists a reversed shape in the bisectors, although WASP-7 seems to be securely located on the "cool" side of this "granulation boundary" (see Figure 17.18 in Gray 2005).

With the present data we cannot determine if one of these or another effect is responsible for the relatively strong variations in the shape of the RM signal. One should therefore view our particular results for the differential rotation, stellar inclination, and the spectroscopic limb-darkening coefficients with some skepticism. Including these effects, or some effects with a similar functional form, is however important for a realistic uncertainty estimation of $v \sin i_\star$ and λ as we will discuss in the next section.

5.2. Stellar Obliquity

As expected from the qualitative discussion we find $\lambda = 86° \pm 6°$, which is consistent with 90°. The projected stellar spin axis is lying nearly within the orbital plane.

We did not use the measurement of the projected rotational velocity ($v \sin i_\star = 17 \pm 2\,\mathrm{km\,s^{-1}}$) by Hellier et al. (2009) as a prior constraint. This is because it is not clear what value of macroturbulence was assumed by those authors, and also because if differential rotation is present then a systematic error could be introduced.

The lack of knowledge on differential rotation and the stellar inclination did lead to an increased confidence interval for λ. This can be seen from the Figures 4 and 9. When the stellar inclination departs from 90°, the planet covers higher stellar latitudes, which have decreased rotational velocities (and therefore a decreased RM effect) either at the beginning or end of the transit. This forces a higher $v \sin i_\star$ and a change in λ to compensate for the asymmetry in the transit RV curve. This degeneracy could be broken if we would have independent information on the stellar inclination.

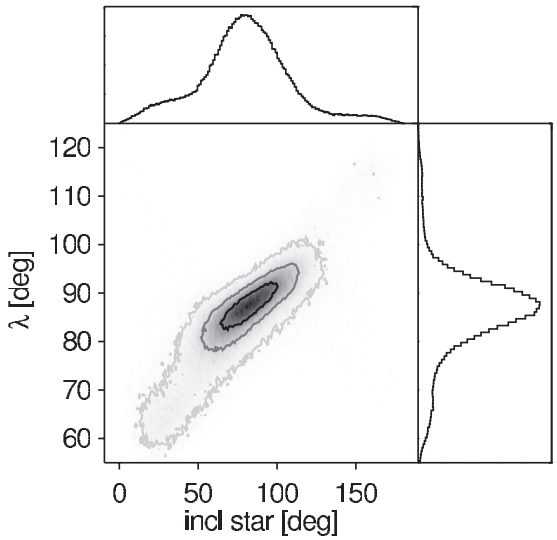

Figure 9. Dependency of λ on $i_\star$. The gray scale indicates the posterior probability density, marginalized over all other parameters. The contours represent the two-dimensional 68.3%, 95%, and 99.73% confidence limits. The one-dimensional marginalized distributions are shown on the sides of the contour plot. One can see the strong correlation between λ and $i_\star$. This correlation vanishes if no differential rotation is present.

To estimate $\sin i_\star$ we can use the technique of Schlaufman (2010), involving a comparison of the measured value of $v \sin i_\star$ with the expected value of v for a star of the given age and mass. Schlaufman found for WASP-7 a rotation statistic $\Theta = -3.4$, indicating that WASP-7 rotates faster than expected for its age and mass. A Θ near 0 would indicate that the measured $v \sin i_\star$ is consistent with the expected rotation speed v for a star of a given mass and age. A Θ larger than 0 would indicate an inclination of the stellar spin axis toward the observer.

We repeat his analysis with the new values for $v \sin i_\star$, found here using the RM effect (Table 2), and the new mass, radius, and age values from Southworth et al. (2011). With these we obtain an expected v of $11 \pm 4\,\mathrm{km\,s^{-1}}$ and a rotation statistic Θ of -0.8. This indicates that the projected rotation speed is consistent with a $\sin i_\star$ of ≈ 1. There is no indication of an inclination of the stellar spin axis toward the observer.

This knowledge could be used as prior knowledge, or more correctly used in the model itself to decrease the uncertainty in the projected obliquity. However, as WASP-7 is at the upper end of the mass range for which Schlaufman (2010) calculated his rotation, mass, age relationship and because of the complications due to differential rotation for which his relation was not calibrated, we decided not to use this knowledge to reduce the uncertainty in λ.

5.3. Stellar Jitter

Analyzing the bisectors of the obtained spectra might lead to a reduced scatter, as was done for HAT-P-33 by Hartman et al. (2011). In particular, the data taken during the transit night might be informative as the change in the bisectors will be correlated over the course of the night.

If during some nights several RVs would have been obtained then the uncertainty in the orbital parameters of WASP-7 could be reduced in a similar approach to that used by Hatzes et al. (2010) for CoRoT-7. They used data obtained during one night to constrain a part of the orbit and allowed for a drift between different nights. However, this approach requires a substantial amount of data and its success depends on the timescale over which the jitter is correlated, with shorter correlation timescales being advantageous.

As we are mainly interested in the systems obliquity we only note here that the relation by Saar et al. (2003) employing a correlation between $v \sin i_\star$ and stellar jitter, leads to an expected jitter of 34 m s^{-1}, similar to the measured value.

6. SUMMARY OF CONCLUSIONS

We find that in the WASP-7 system the stellar spin axis is strongly misaligned with the planet's orbital axis, by $86^\circ \pm 6^\circ$ as projected on the sky. This observation strengthens the correlation found by Winn et al. (2010) and lends support to the idea that systems with close giant planets generally started out with a very broad range of obliquities, and that the observed low obliquities of many systems are a consequence of tidal dissipation.

Differential rotation and its imprint on the RM effect holds the promise of measuring not only the projections of stellar obliquities, but also the stellar inclinations. However, with the current measurement precision and uncertainties in other parameters such as limb darkening, no secure detection of differential rotation in WASP-7 can be made. We originally thought that WASP-7 might present a good test bed to search for differential rotation via the RM effect, as the misalignment of 90° maximizes the RM signal originating from differential rotation. However for this angle the signal from differential rotation is also strongly correlated with stellar limb darkening. In addition WASP-7 displays a high degree of stellar jitter. Therefore, a system with a quiet star and a more moderate misalignment might be better suited to search for signs of differential rotation in the RM signal.

S.A. thanks the Harvard-Smithsonian Center for Astrophysics, where this manuscript was begun, for its hospitality. S.A. acknowledges support by a Rubicon fellowship from the Netherlands Organization for Scientific Research (NWO) during parts of this project. J.N.W. acknowledges support from a NASA Origins grant (NNX09AD36G). T.H. is supported by Japan Society for Promotion of Science (JSPS) Fellowship for Research (DC1: 22-5935). This research has made use of the Simbad database located at http://simbad.u-strasbg.fr/.

REFERENCES

Albrecht, S., Reffert, S., Snellen, I., Quirrenbach, A., & Mitchell, D. S. 2007, A&A, 474, 565
Albrecht, S., Winn, J. N., Johnson, J. A., et al. 2011, ApJ, 738, 50
Butler, R. P., Marcy, G. W., Williams, E., et al. 1996, PASP, 108, 500
Chatterjee, S., Ford, E. B., Matsumura, S., & Rasio, F. A. 2008, ApJ, 686, 580
Claret, A. 2004, A&A, 428, 1001
Collier Cameron, A., Bruce, V. A., Miller, G. R. M., Triaud, A. H. M. J., & Queloz, D. 2010, MNRAS, 403, 151
Crane, J. D., Shectman, S. A., Butler, R. P., et al. 2010, Proc. SPIE, 7735, 170
Cresswell, P., Dirksen, G., Kley, W., & Nelson, R. P. 2007, A&A, 473, 329
Fabrycky, D., & Tremaine, S. 2007, ApJ, 669, 1298
Gaudi, B. S., & Winn, J. N. 2007, ApJ, 655, 550
Gray, D. F. 1984, ApJ, 281, 719
Gray, D. F. 2005, The Observation and Analysis of Stellar Photospheres (3rd ed.; Cambridge: Cambridge Univ. Press)
Hartman, J. D., Bakos, G. Á., Torres, G., et al. 2011, ApJ, 742, 59
Hatzes, A. P., Dvorak, R., Wuchterl, G., et al. 2010, A&A, 520, A93
Hébrard, G., Bouchy, F., Pont, F., et al. 2008, A&A, 488, 763
Hellier, C., Anderson, D. R., Gillon, M., et al. 2009, ApJ, 690, L89
Hirano, T., Narita, N., Sato, B., et al. 2011a, arXiv:1108.4493
Hirano, T., Suto, Y., Taruya, A., et al. 2010, ApJ, 709, 458
Hirano, T., Suto, Y., Winn, J. N., et al. 2011b, arXiv:1108.4430
Johnson, J. A., Winn, J. N., Albrecht, S., et al. 2009, PASP, 121, 1104
Laughlin, G., Marcy, G. W., Vogt, S. S., Fischer, D. A., & Butler, R. P. 2005, ApJ, 629, L121
Lin, D. N. C., Bodenheimer, P., & Richardson, D. C. 1996, Nature, 380, 606
Mandel, K., & Agol, E. 2002, ApJ, 580, L171
Maxted, P. F. L., Koen, C., & Smalley, B. 2011, MNRAS, 418, 1039
Nagasawa, M., Ida, S., & Bessho, T. 2008, ApJ, 678, 498
Ohta, Y., Taruya, A., & Suto, Y. 2005, ApJ, 622, 1118
Pont, F., Husnoo, N., Mazeh, T., & Fabrycky, D. 2011, MNRAS, 414, 1278
Reiners, A., & Schmitt, J. H. M. M. 2003, A&A, 398, 647
Saar, S. H., Hatzes, A., Cochran, W., & Paulson, D. 2003, in The Future of Cool-Star Astrophysics: 12th Cambridge Workshop on Cool Stars, Stellar Systems, and the Sun, Vol. 12, ed. A. Brown, G. M. Harper, & T. R. Ayres (Boulder, CO: Univ. Colorado), 694
Schlaufman, K. C. 2010, ApJ, 719, 602
Shporer, A., & Brown, T. 2011, ApJ, 733, 30
Simpson, E. K., Pollacco, D., Cameron, A. C., et al. 2011, MNRAS, 414, 3023
Southworth, J., Dominik, M., Jørgensen, U. G., et al. 2011, A&A, 527, A8
Triaud, A. H. M. J. 2011, A&A, 534, L6
Triaud, A. H. M. J., Collier Cameron, A., Queloz, D., et al. 2010, A&A, 524, A25
Winn, J. N., Fabrycky, D., Albrecht, S., & Johnson, J. A. 2010, ApJ, 718, L145
Winn, J. N., Howard, A. W., Johnson, J. A., et al. 2011, AJ, 141, 63
Winn, J. N., Johnson, J. A., Albrecht, S., et al. 2009, ApJ, 703, L99